SCIENTIFIC REPORTS
nature research

OPEN

Raman Spectra Shift of Few-Layer IV-VI 2D Materials

Minwoo Park[1,2], Jin Sik Choi[2], Li Yang[1*] & Hoonkyung Lee[2*]

Raman spectroscopy is the most commonly used method to investigate structures of materials. Recently, few-layered IV-VI 2D materials (SnS, SnSe, GeS, and GeSe) have been found and ignited significant interest in electronic and optical applications. However, unlike few-layer graphene, in which its interlayer structures such as the number of its layers are confirmed through measurement of the Raman scattering, few-layer IV-VI 2D materials have not yet been developed to the point of understanding their interlayer structure. Here we performed first-principles calculations on Raman spectroscopy for few-layer IV-VI 2D materials. In addition to achieving consistent results with measurements of bulk structures, we revealed significant red and blue shifts of characteristic Raman modes up to 100 cm^{-1} associated with the layer number. These shifts of lattice vibrational modes originate from the change of the bond lengths between the metal atoms and chalcogen atoms through the change of the interlayer interactions. Particularly, our study shows weak covalent bonding between interlayers, making the evolution of Raman signals according to the thickness different from other vdW materials. Our results suggest a new way for obtaining information of layer structure of few-layer IV-VI 2D materials through Raman spectroscopy.

Recently, van der Waals (vdW) materials such as graphene and transition metal dichalcogenides have attracted substantial attention from nanoscience and technology fields because they have exotic electronic properties and potential applications for energy storage and harvest. In addition, their properties have been shown to be dependent on the number of layers they have[1–6]. For example, for graphene, it has a Dirac cone in a single layer while it is gone more than one layer, leading to different physical phenomena such as massless and mass Fermions, respectively[7,8]. Bilayer graphene shows an exotic superconducting phase as the twisting angle between the layers[9]. By contrast, single-layer MoS_2 is semiconducting with a direct bandgap of 1.57 eV, and the properties of few-layer MoS_2 are significantly tuned to be indirect-bandgap semiconductors by the number of layers, because of interlayer interaction[10–12]. Although the technology for controlling the thickness of vdW materials has been developed by exfoliation and atomic layer deposition methods[13–18], it is highly appreciated to conveniently verify the number of layers or thicknesses of vdW materials for device applications.

As one of the most fundamental tools to study structures, Raman spectroscopy can be employed to determine the thickness of few-layer vdW materials such as graphene[19] and transition metal dichalcogenides[20] because the lattice vibration modes are dependent on the number of layers of the vdW materials. For instance, for graphene, the number of layers can be determined based on the results of Raman spectroscopy: the change of the position of G peak or the position and shape of the 2D band[21]. In the case of MoS_2, the positions of the $E^1{}_{2g}$ and A_{1g} peaks provide clues for the thickness[22–24]. For black phosphorus, the intensities of $A_g{}^1$ and B_{2g} peaks play the same roles[25].

More recently, in few-layer metal monochalcogenides (MX, M = Sn, Ge; X = S, Se, etc.), members of layered IV-VI compounds have been discovered through exfoliation from bulk structures[26–28]. The structures are the same as that of black phosphorus, which is called the puckered structure, where M and X are bonded alternatively (Fig. 1). These novel materials show intriguing electric polarization properties[26,27,29,30]. In addition, they have properties of vertical dielectric screening, resulting in changes to the electronic and optical properties[27,31,32]. On the other hand, due to their high absorption coefficient, they can be used for photovoltaic cells[3,33–38] and show high performance. They can also be used for lithium-ion battery anodes[39,40], because they have layered structures where Li are intercalated to space between layers, exhibiting high Li capacity. In addition, MX has attracted much attention due to the ~1 eV electronic bandgap close to bulk silicon. Thus MX has a huge potential for use in electric devices[41]. Similar to almost layer stacking structures, monolayer or few-layer MX could have a distinctive property or better performance for certain devices, like thin-film devices[42]. Recently, there have been many attempts to synthesize few-layer MX, including through the CVD method[43–48], chemical bath deposition[38,49,50],

[1]Department of Physics, Washington University in St. Louis, St. Louis, Missouri, 63136, USA. [2]Department of Physics, Konkuk University, Seoul, 05029, Korea. *email: lyang@physics.wustl.edu; hkiee3@konkuk.ac.kr

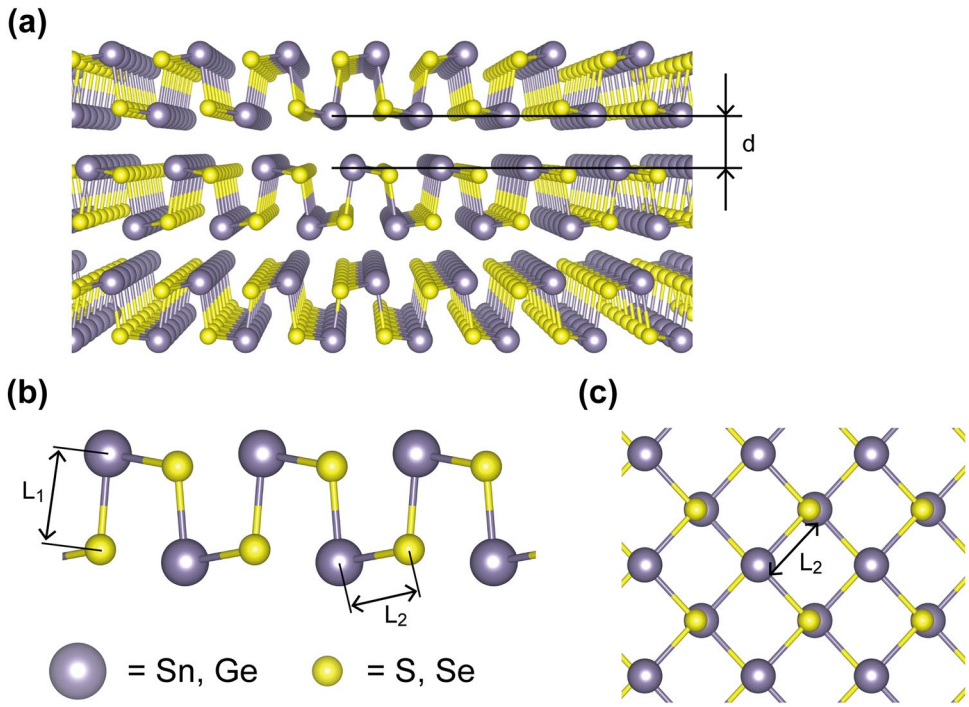

Figure 1. (**a**) Schematic diagram of the crystal structure of MX. It is a puckered structure like that of black phosphorus. *d* denotes the interlayer distance. (**b**) L_1 and L_2 represent bonding lengths of the vertical and horizontal directions of the plane, respectively. (**c**) Top view of the crystal structure.

atomic layer deposition[18,51], and spray pyrolysis[52]. Heterostructures with MX have also been studied as field-effect transistor device materials[48].

However, like graphene and transition metal dichalcogenides, verifying the number of layers in few-layer MX structures is crucial when they are used as device materials. In stacking a layer, we average the length of all similar direction bonding. While MX has attracted great interest, verifying the number of layers of MX sample has not yet been sufficiently studied. For example, there has only been one case verifying the thickness of a sample using an electronic bandgap[10]; that is a good method for figuring out the thickness. However, measuring a bandgap has too many more steps than Raman and can ruin an exfoliated crystal sample. Therefore, nondestructive Raman method might be the best method, but there are no relevant reference data. In this paper, we performed Raman simulation for MX as the number of layers varied from a monolayer to bulk in order to provide standard Raman spectroscopy data. We focus on SnS, SnSe, GeS, and GeSe as representative examples for MX. Our calculations show that the Raman spectroscopy for metal monochalcogenides depends on the number of layers. We found that the red shift and blue shift occur continuously as the number of layers increases by ~100 cm^{-1}. This can be explained by the fact that the shifts come from the change of the bond lengths between the metal atoms and chalcogen atoms by the change of the interlayer interaction, leading to the slight modification of a vibration mode. These results provide benchmarks for determining the number of layers of metal monochalcogenides by Raman spectroscopy analysis.

All of the calculations were carried out using density functional theory (DFT) and density functional perturbation theory (DFPT)[53], as implemented in the PWSCF package of the QUANTUM-ESPRESSO[54]. The DFT is employed for the geometry optimization of the IV-VI layers, and the DFPT is employed for calculations of the Raman spectra, phonons, and dynamical matrices. We used norm conserved local density approximation (LDA) for pseudopotentials[55,56], which gives consistent results with PBE-D3. The kinetic energy cutoff was taken to be 30 Ry. We use $9 \times 9 \times 3$ and $9 \times 9 \times 1$ k-point for the bulk and layered structures, respectively. Geometrical optimizations are performed for every single structure until the Hellman-Feynman force is below 10^{-8} Ry/Bohr. All of our calculations were converged to ~10^{-4} Ry/atom. Detail information for the optimization of the lattice vectors and the lattice constants is described in supporting information Figure S1, Figure S2, and Table S1.

We first performed calculations on the geometry optimizations for AB staked multilayered MXs (Fig. 1a) because it has been confirmed that, for MX bulks, AB stacked MX layers in bulks are the energetically most favorable configuration[57,58]. Figure 1 shows the optimized atomics structures of AB-stacked multilayer MX structures, where L_1 and L_2 denote the bonding lengths for out of plane and in-plane, respectively. The calculated values of the L_1 and L_2 and the interlayer distances for AB stacked MX multilayers are presented in Table 1, which are consistent with the values in the literature for a multi-layer[59]. For instance, L_1 and L_2 were calculated to be 2.56 and 2.70 Å for bilayer SnS, respectively. The bond lengths are increased as the atomic numbers of M and X increase. However, the interlayer distance, *d* is 2.64 Å (Supporting information Figure S3), slightly dependent on the type of MX layers, which corresponds to the equilibrium distance of ~3.4 Å via vdW interaction. Furthermore, the calculated values of L_1, L_2, and *d* as the number of layers varied from 1 to 3 are also presented

Materials	# of layers	L_1	L_2	Δ_1	Δ_2	d
SnS	1	2.53	2.73	0	0	—
	2	2.56	2.70	0.03	−0.03	2.64
	3	2.58	2.69	0.05	−0.04	2.64
	∞	2.61	2.64	0.08	−0.09	2.57
SnSe	1	2.66	2.91	0	0	—
	2	2.69	2.84	0.03	−0.07	2.79
	3	2.70	2.79	0.04	−0.12	2.71
	∞	2.75	2.77	0.09	−0.14	2.66
GeS	1	2.36	2.46	0	0	—
	2	2.39	2.45	0.03	−0.01	2.49
	3	2.39	2.44	0.03	−0.02	2.46
	∞	2.43	2.42	0.07	−0.04	2.36
GeSe	1	2.49	2.59	0	0	—
	2	2.51	2.59	0.02	0	2.80
	3	2.52	2.56	0.03	−0.03	2.58
	∞	2.55	2.56	0.06	−0.03	2.51

Table 1. Calculated local geometry information for AB stacked MX layers as the number of layers. $\Delta_1(\Delta_2)$ denotes L_1 (L_2) for a given layer minus L_1 (L_2) of monolayer presented in Fig. 1(b). The unit of the values below is angstroms. ∞ means multilayer of MX. d indicates the interlayer distance.

Functionals	# of layers	SnS	SnSe	GeS	GeSe
LDA	2	$E_b = 0.50$ eV	0.50 eV	0.49 eV	0.38 eV
		$d = 2.64$ Å	2.79 Å	2.49 Å	2.80 Å
	3	$E_b = 0.46$ eV	0.51 eV	0.49 eV	0.39 eV
		$d = 2.64$ Å	2.71 Å	2.46 Å	2.58 Å
Meta-GGA	2	$E_b = 0.26$ eV	0.26 eV	0.28 eV	0.28 eV
		$d = 2.97$ Å	3.15 Å	2.73 Å	3.04 Å

Table 2. Calculated binding energy (E_b) between interlayers for few-layer MXs and interlayer distance (d). The exchange-correlation functional is treated using LDA and strongly constrained and appropriately normed (SCAN) meta-generalized gradient approximation (meta-GGA).

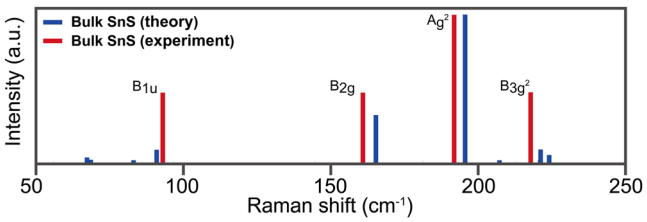

Figure 2. Calculated and experimental Raman spectroscopy for AB stacked multilayer SnS. The experimental data was in ref. [62].

in Table 1. We also carried out the calculations on the interlayer binding energy of bilayer and trilayer MXs in Table 2. For comparison, the interlayer binding energy and the interlayer distance were also calculated with other functional, i.e., meta-GGA[60]. The binding energy and the interlayer distance obtained with the LDA is slightly larger and smaller than those with the meta-GGA, respectively. We found that there are small changes in L_1 and L_2 as well as interlayer distance, similar to other 2D materials[12,61].

We performed calculations on the Raman spectra of multilayer MX using DFPT calculation. In order to verify the computational accuracy of the DFPT, the calculated results were compared to the experimental data for AB stacked multilayer SnS[18]. We focused on the four characteristic peaks in the spectra of 53, 76, 104, and 244 cm^{-1} for monolayer SnS, because their Raman signals are remarkable and have been observed in experiments[18,62]. Remarkably, the calculated Raman spectra for SnS is strongly consistent with the experimental data (Fig. 2)[18]. Thus, we believe that our calculations on the Raman spectra for other MX layers are reliable for predicting their properties. Moreover, it was verified that there is high accuracy in Raman simulations for monolayer using the ab initio method[63].

We further analyzed the lattice vibrational modes of AB-stacked multilayer SnS corresponding to the characteristic Raman peaks in order to determine how the peaks are generated. We found that the phonon modes of

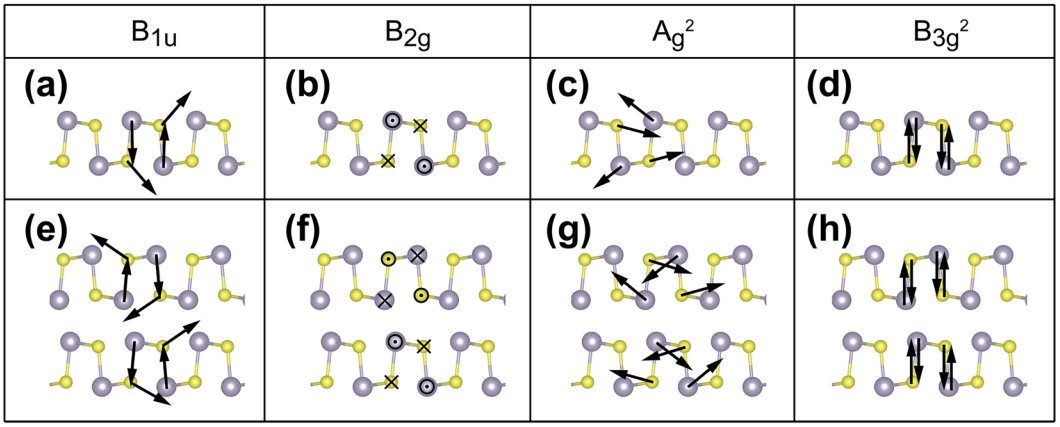

Figure 3. Phonon modes of monolayer ((**a**–**d**)) and multilayer (**e**–**h**) SnS: B_{1u}, B_{2g}, A_g^2, and B_{3g}^2.

the four B_{1u}, A_g^2, B_{2g}, and B_{3g}^2 shown in Fig. 3(e–h), respectively, are associated with the peaks for 91, 166, 196, and 221 cm^{-1} for multilayer SnS, respectively. Hereafter, we refer to the four peaks in the Raman spectra as B_{1u}, A_g^2, B_{2g}, and B_{3g}^2, respectively. Monolayer SnS has the same phonon modes in Fig. 3(a–d). For the B_{1u} phonon mode, Sn atoms move out of plane and S atoms move in the oblique plane (Fig. 3(a,e)). For the A_g^2 phonon mode, Sn and S atoms move in the oblique plane (Fig. 3(c,g)). For the B_{2g}, and B_{3g}^2 phonon modes, the Sn and S atoms move in the same plane in the opposite direction (Fig. 3(b,d,f,h)). These modes can be approximately classified by atomic moving direction into three kinds: vertical of the MX plane, horizontal of the MX plane, and hybrid. B_{2g} is horizontal while B_{3g}^2 is vertical of the SnS plane. B_{1u} looks like a hybrid of the two. In A_g^2 mode, atoms have a vibration in both directions, out of plane and in-plane. However, moving in out of plane appears to be negligible. Therefore, we can classify A_g^2 as the horizontal mode.

In order to investigate how the Raman spectra of few-layer MX materials depend on the number of layers, we performed calculations for few-layers MX as the number of layers varied. An attractive feature is that the Raman spectrum of SnS is dependent on the number of layers. For SnS, we found that B_{1u}, B_{2g}, and A_g^2 are a blue shift by ~40 cm^{-1}, ~90 cm^{-1}, and ~92 cm^{-1}, respectively, while B_{3g}^2 are red shift by ~23 cm^{-1}.(Fig. 4(a)) Since Raman peaks are naturally split by stacking layers, we selected the most significant peak among several split peaks. If certain peaks are degenerate in the same position, the measured intensity is higher than that of the theoretical prediction. Increasing the number of layers yields a red shift for B_{3g}^2 and a blue shift for B_{2g} and A_g^2. These trends appear in all four MX except for B_{1u}. For the SnS and GeS layers, the B_{1u} mode shows a blue shift. For GeSe, the B_{1u} mode has a red shift trend, while it does not show any shift trend for SnSe. For other peaks, the changes appear to be sufficient to distinguish the number of layers of samples. On the other hand, the interaction addition as the number of layers is significant in a vertical direction compared with a horizontal direction because The thickness with respect to the vertical to the plane of MXs is increased as the number of their layers increases because L_1 increases as the number of layers increases (see Table 1). Therefore, the frequency shift in a complete vertical mode, i.e., B_{3g}^2 is more significant than that other modes as shown in Fig. 4.

Moreover, we observe that the tendency depends on the direction of phonon mode, horizontal or vertical. In Fig. 5, the horizontal modes (such as B_{2g}), in-plane modes, appear as the blue shift tendency, while the vertical modes (such as B_{3g}^2), out of plane modes, appear as the red shift trend when increasing the number of layers for SnS. This relation is consistent across the four kinds of MX.

We investigate what causes the difference between red and blue shift trends. In order to determine the blue and red shifts of the Raman spectroscopy, we investigated the local geometry of them with varying numbers of layers. The calculated values of the bond lengths (L_1, L_2) between L_1, L_2, and interlayered distance as the number of layers varies are presented in Table 1. Importantly, we found that there is a small change of length for unit cell vectors, as in other 2D materials[12,61]. Further, there are certain changes of atomic bonding length from interlayer interactions. This can change the lattice vibration motion, which might be one of the causes of the shift tendency. We can understand that the change of bond lengths can be interpreted by the change of the spring constant using a simple harmonic approximation. Hence, when a bonding length is decreasing, a frequency is increased. This is the reason for why Raman shift frequency, a peak position, is changed according to the number of layers. According to the number of layers, the changes for L_1 and L_2 are shown in Table 1. With increasing the number of layers, L_1, an average bond length of the vertical direction, is increasing, while L_2, an average bond length of the horizontal direction, is decreasing. In other words, with increasing the number of layers, the vertical mode has a red shift and the horizontal mode has a blue shift. This relation holds for all our studied MXs.

In order to understand the origin of the bond lengths of few-layer MXs resulting in the shift of the phonon energy, we investigate the bond between layers. We found that this change of the lattice parameter via the interaction between layers stems from the weakly covalent bonding between interlayers, as shown in Fig. 6, where the charges transfer between interlayers. This differs from the bond between interlayer of few-layer vdW materials like graphene or MoS_2. In addition, the binding energy of the layers is calculated to range from 0.2 eV to 0.5 eV, slightly dependent on the type of sheets (Table 2), which is greater than the value of a few ten meV in graphite and MoS_2[64–66]. This result is consistent with those of previous studies[67,68]. Therefore, we believe that, because of the stronger interaction between layers than other vdW materials, the Raman shifts as the number of layers occur.

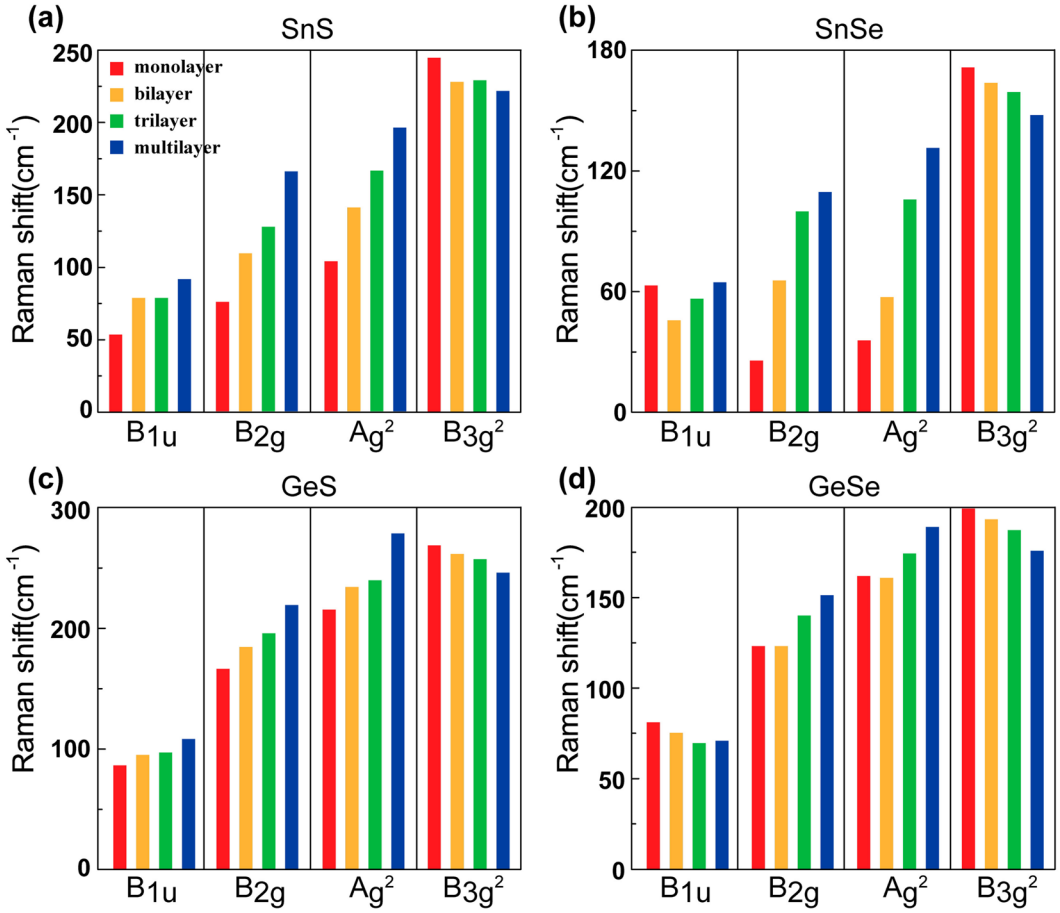

Figure 4. Raman shifts for four peaks in (**a**) SnS, (**b**) SnSe, (**c**) GeS, and (**d**) GeSe as the number of layers. With an increasing number of layers, Raman shifts increase or decrease depending on the type of phonon mode.

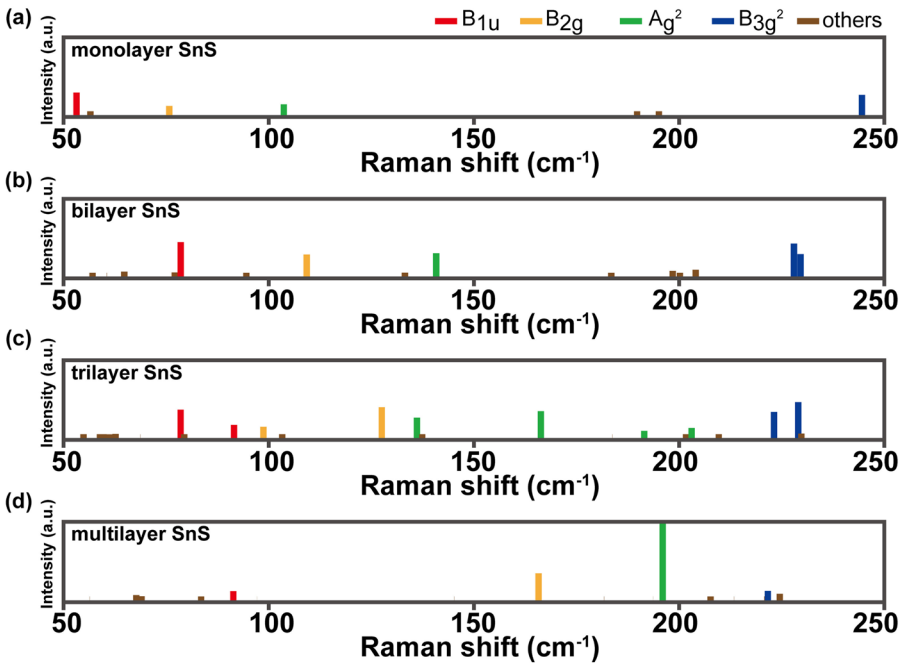

Figure 5. Calculated Raman spectroscopy of AB stacked few-layered SnS as the number of layers: (**a**) monolayer, (**b**) bilayer, (**c**) trilayer, and (**d**) multilayer SnS.

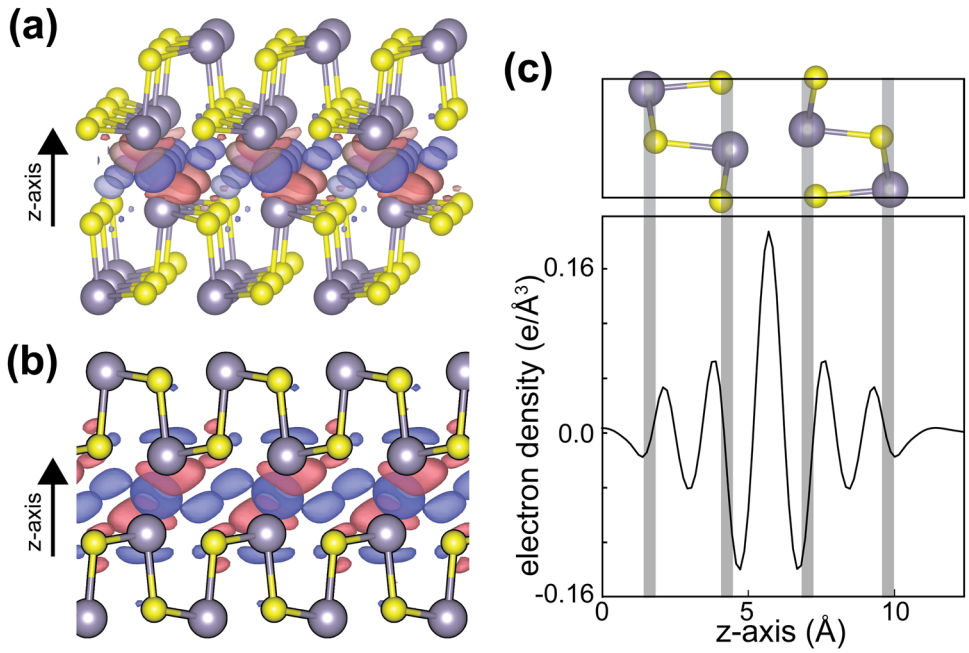

Figure 6. Calculated charge density difference between interlayers: (**a**) Oblique view (**b**) Side view. The red and blue colors indicate the accumulation and depletion of electrons, respectively. (**c**) In-plane projected charge density along with z direction.

	B_{1u}	B_{2g}	A_g^2	B_{3g}^2
SnS	(−37.7, 92.5)	(−88.9, 160.2)	(−93.3, 194.3)	(22.6, 220.3)
SnSe	(−1.2, 58.0)	(−88.3, 115.6)	(−99.4, 128.0)	(23.4, 149.6)
GeS	(−21.4, 106.8)	(−52.2, 215.6)	(−59.9, 269.8)	(21.9, 248.3)
GeSe	(11.2, 69.1)	(−28.8, 148.0)	(−26.8, 184.3)	(23.0, 178.4)

Table 3. Coefficients (a_i, b_i) to Eq. (1) for each phonon mode. The unit of the values below is cm^{-1}.

The relation between Raman shifts ($\Delta\nu$ (cm^{-1})) and the number of layers for MXs is shown in Fig. 4. We confirmed that this relationship remains very consistent for A_g^2, B_{3g}^2, and B_{2g}. The data could almost be fitted linearly by a reciprocal number of layers as follows:

$$\Delta\nu_i\ (\mathrm{cm}^{-1}) = \frac{a_i}{N} + b_i, \tag{1}$$

where the subscript i indicates the index of phonon modes, a_i and b_i are fitting coefficients for a given i and N indicates the number of MX layers. The calculated coefficients for MX layers were calculated by a linear fitting (Supporting information Figure S1), which are presented in Table 3. The negative and positive values of a_i mean red and blue shifts as N increases, respectively. This will be very beneficial in experiments to know the number of layers for a sample. Even though some shifts are of a small value per layer, like GeSe, modern Raman equipment has sufficient resolution ($<1\ cm^{-1}$) in room temperature to identify them[69]. In addition, for all examples, there are more than two rapid shift peaks, enough to identify thickness. The blue shift peaks, the horizontal modes, might be useful indicators for verifying the number of layers for almost MX. Another important point is that we propose a method of distinguishing the number of layers by comparing predicted Raman shift using Eq. (1) with experimental results of the Raman spectrum.

In conclusion, we have done the first-principles calculations for Raman spectroscopy based on the density functional theory. We found important things for a shift of the Raman peaks of metal monochalcogenide (MX), as its the number of layers. (1) Raman spectroscopy is considerably dependent upon the number of layers. (2) We have discovered the shifting or red trend of Raman peaks as the number of layers due to the change in atomic bonding length along with the direction of phonon. (3) We believe that our graphs for Raman peaks are useful benchmarks for identifying the number of layers of an arbitrary MX sample. Our results propose a method for distinguishing the number of layers in recently-reported few-layer MXs.

Received: 28 June 2019; Accepted: 21 November 2019;
Published online: 20 December 2019

References

1. Peng, Q. & De, S. Outstanding mechanical properties of monolayer MoS2 and its application in elastic energy storage. *Phys. Chem. Chem. Phys.* **15**, 19427–37 (2013).
2. Baugher, B. W., Churchill, H. O., Yang, Y. & Jarillo-Herrero, P. Intrinsic Electronic Transport Properties of High-Quality Monolayer and Bilayer MoS2. *Nano Lett.* **13**, 4212–4216 (2013).
3. Xia, C. *et al*. A type-II GeSe/SnS heterobilayer with a suitable direct gap, superior optical absorption and broad spectrum for photovoltaic applications. *J. Mater. Chem. A Mater* **5**, 13400–13410 (2017).
4. Chen, X. & Xia, F. Black phosphorous optoelectronic devices. *Proc.of SPIE* **10194**, 101940E (2017).
5. Miranda, H. P. C. *et al*. Quantum Interference Effects in Resonant Raman Spectroscopy of Single- and Triple-Layer MoTe2from First-Principles. *Nano Lett.* **17**, 2381–2388 (2017).
6. Favron, A. *et al*. Photooxidation and quantum confinement effects in exfoliated black phosphorus. *Nat. Mater.* **14**, 826–832 (2015).
7. Zhang, Y. *et al*. Direct observation of a widely tunable bandgap in bilayer graphene. *Nature* **459**, 820–823 (2009).
8. Mucha-Kruczyński, M. *et al*. Characterization of graphene through anisotropy of constant-energy maps in angle-resolved photoemission. *Phys. Rev. B* **77**, 195403–12 (2008).
9. Cao, Y. *et al*. Unconventional superconductivity in magic-angle graphene superlattices. *Nature* **556**, 43–50 (2018).
10. Brent, J. R. *et al*. Tin(II) Sulfide (SnS) Nanosheets by Liquid-Phase Exfoliation of Herzenbergite: IV–VI Main Group Two-Dimensional Atomic Crystals. *J. Am. Chem. Soc.* **137**, 12689–12696 (2015).
11. Zhang, S. *et al*. Two-dimensional GeS with tunable electronic properties via external electric field and strain. *Nanotechnology* **27**, 274001 (2016).
12. Ahmad, S. & Mukherjee, S. A Comparative Study of Electronic Properties of Bulk MoS2 and Its Monolayer Using DFT Technique: Application of Mechanical Strain on MoS2 Monolayer. *Graphene* **3**, 52–59 (2014).
13. Johnson, R. W., Hultqvist, A. & Bent, S. F. A brief review of atomic layer deposition: from fundamentals to applications. *Mater. Today* **17**, 236–246 (2014).
14. Miikkulainen, V., Leskelä, M., Ritala, M. & Puurunen, R. L. Crystallinity of inorganic films grown by atomic layer deposition: Overview and general trends. *J. Appl. Phys.* **113**, 021301–102 (2013).
15. Song, L. *et al*. Large Scale Growth and Characterization of Atomic Hexagonal Boron Nitride Layers. *Nano Lett.* **10**, 3209–3215 (2010).
16. Geim, A. K. & Grigorieva, I. V. Van der Waals heterostructures. *Nature* **499**, 419–425 (2013).
17. Jaramillo, R. *et al*. Making Record-efficiency SnS Solar Cells by Thermal Evaporation and Atomic Layer Deposition. *J. Vis. Exp.* e52705 (2015).https://doi.org/10.3791/52705
18. Sinsermsuksakul, P., Heo, J., Noh, W., Hock, A. S. & Gordon, R. G. Atomic Layer Deposition of Tin Monosulfide Thin Films. *Adv. Energy Mater* **1**, 1116–1125 (2011).
19. Tan, P. H. *et al*. The shear mode of multilayer graphene. *Nature Mater* **11**, 294–300 (2012).
20. Zhang, X. *et al*. Raman spectroscopy of shear and layer breathing modes in multilayer MoS2. *Phys. Rev. B* **87**, 115413 (2013).
21. Ferrari, A. C. Raman spectroscopy of graphene and graphite: Disorder, electron–phonon coupling, doping and nonadiabatic effects. *Solid State Commun* **143**, 47–57 (2007).
22. Li, H. *et al*. From Bulk to Monolayer MoS2: Evolution of Raman Scattering. *Adv. Funct. Mater.* **22**, 1385–1390 (2012).
23. Lee, C. *et al*. Anomalous Lattice Vibrations of Single- and Few-Layer MoS2. *ACS Nano* **4**, 2695–2700 (2010).
24. Zhang, X. *et al*. Phonon and Raman scattering of two-dimensional transition metal dichalcogenides from monolayer, multilayer to bulk material. *Chem. Soc. Rev.* **44**, 2757–2785 (2015).
25. Castellanos-Gomez, A. *et al*. Isolation and characterization of few-layer black phosphorus. *2D Mater* **1**, 025001 (2014).
26. Mehboudi, M. *et al*. Structural Phase Transition and Material Properties of Few-Layer Monochalcogenides. *Phys. Rev. Lett.* **117**, 246802–5 (2016).
27. Koteeswara Reddy, N., Devika, M. & Gopal, E. S. R. Review on Tin (II) Sulfide (SnS) Material: Synthesis, Properties, and Applications. *Crit. Rev. Solid State Mater. Sci* **40**, 359–398 (2015).
28. Wu, L. *et al*. Few-Layer Tin Sulfide: A Promising Black-Phosphorus-Analogue 2D Material with Exceptionally Large Nonlinear Optical Response, High Stability, and Applications in All-Optical Switching and Wavelength Conversion. *Adv. Opt. Mater.* **6**, 1700985–10 (2017).
29. Fei, R., Li, W., Li, J. & Yang, L. Giant piezoelectricity of monolayer group IV monochalcogenides: SnSe, SnS, GeSe, and GeS. *Appl. Phys. Lett.* **107**, 173104–6 (2015).
30. Fei, R., Kang, W. & Yang, L. Ferroelectricity and Phase Transitions in Monolayer Group-IV Monochalcogenides. *Phys. Rev. Lett.* **117**, 097601–6 (2016).
31. Gomes, L. C., Carvalho, A. & Castro Neto, A. H. Enhanced piezoelectricity and modified dielectric screening of two-dimensional group-IV monochalcogenides. *Phys. Rev. B* **92**, 214103 (2015).
32. Chowdhury, C., Karmakar, S. & Datta, A. Monolayer Group IV–VI Monochalcogenides: Low-Dimensional Materials for Photocatalytic Water Splitting. *J. Phys. Chem. C* **121**, 7615–7624 (2017).
33. Devika, M., Reddy, N. K. & Gunasekhar, K. R. Structural, electrical, and optical properties of as-grown and heat treated ultra-thin SnS films. *Thin Solid Films* **520**, 628–632 (2011).
34. Franzman, M. A., Schlenker, C. W., Thompson, M. E. & Brutchey, R. L. Solution-Phase Synthesis of SnSe Nanocrystals for Use in Solar Cells. *J. Am. Chem. Soc.* **132**, 4060–4061 (2010).
35. Shi, G. & Kioupakis, E. Anisotropic Spin Transport and Strong Visible-Light Absorbance in Few-Layer SnSe and GeSe. *Nano Lett.* **15**, 6926–6931 (2015).
36. Loferski, J. J. Theoretical Considerations Governing the Choice of the Optimum Semiconductor for Photovoltaic Solar Energy Conversion. *J. Appl. Phys.* **27**, 777–784 (1956).
37. Sinsermsuksakul, P. *et al*. Overcoming Efficiency Limitations of SnS-Based Solar Cells. *Adv. Energy Mater* **4**, 1400496–7 (2014).
38. Reghima, M., Akkari, A., Guasch, C., Castagné, M. & Kamoun-Turki, N. Synthesis and characterization of Fe-doped SnS thin films by chemical bath deposition technique for solar cells applications. *J. Renew. Sustain. Energy* **5**, 063109–11 (2013).
39. Im, H. S. *et al*. Germanium and Tin Selenide Nanocrystals for High-Capacity Lithium Ion Batteries: Comparative Phase Conversion of Germanium and Tin. *J. Phys. Chem. C* **118**, 21884–21888 (2014).
40. Kim, Y. *et al*. SnSe alloy as a promising anode material for Na-ion batteries. *Chem. Commun.* **51**, 50–53 (2014).
41. Chandrasekhar, H. R., Humphreys, R. G., Zwick, U. & Cardona, M. Infrared and Raman spectra of the IV-VI compounds SnS and SnSe. *Phys. Rev. B* **15**, 2177 (1977).
42. Zhang, C. *et al*. Two-Dimensional Tin Selenide Nanostructures for Flexible All-Solid-State Supercapacitors. *ACS Nano* **8**, 3761–3770 (2014).
43. Kevin, P., Lewis, D. J., Raftery, J., Malik, M. A. & O'Brien, P. Thin films of tin(II) sulphide (SnS) by aerosol-assisted chemical vapour deposition (AACVD) using tin(II) dithiocarbamates as single-source precursors. *J. Cryst. Growth* **415**, 93–99 (2015).
44. Kana, A. T. *et al*. Organotin unsymmetric dithiocarbamates: synthesis, formation and characterisation of tin(II) sulfide films by atmospheric pressure chemical vapour deposition. *Polyhedron* **20**, 2989–2995 (2001).
45. Ramasamy, K. *et al*. Organotin Dithiocarbamates: Single-Source Precursors for Tin Sulfide Thin Films by Aerosol-Assisted Chemical Vapor Deposition (AACVD). *Chem. Mater.* **25**, 266–276 (2013).

46. Hibbert, T. G., Mahon, M. F., Molloy, K. C., Price, L. S. & Parkin, I. P. Deposition of tin sulfide thin films from novel, volatile (fluoroalkythiolato)tin(iv) precursors. *J. Mater. Chem.* **11**, 469–473 (2001).
47. Bade, B. P., Garje, S. S., Niwate, Y. S., Afzaal, M. & O'Brien, P. Tribenzyltin(IV)chloride Thiosemicarbazones: Novel Single Source Precursors for Growth of SnS Thin Films. *Chem. Vap. Deposition* **14**, 292–295 (2008).
48. Sánchez-Juárez, A., Tiburcio-Silver, A. & Ortiz, A. Fabrication of SnS2/SnS heterojunction thin film diodes by plasma-enhanced chemical vapor deposition. *Thin Solid Films* **480–481**, 452–456 (2005).
49. Ray, S. C., karanjai, M. K. & DasGupta, D. Structure and photoconductive properties of dip-deposited SnS and SnS2 thin films and their conversion to tin dioxide by annealing in air. *Thin Solid Films* **350**, 72–78 (1999).
50. Gao, C. & Shen, H. Influence of the deposition parameters on the properties of orthorhombic SnS films by chemical bath deposition. *Thin Solid Films* **520**, 3523–3527 (2012).
51. Kim, J. Y. & George, S. M. Tin Monosulfide Thin Films Grown by Atomic Layer Deposition Using Tin 2,4-Pentanedionate and Hydrogen Sulfide. *J. Phys. Chem. C* **114**, 17597–17603 (2010).
52. Koteswara Reddy, N. & Ramakrishna Reddy, K. T. Growth of polycrystalline SnS films by spray pyrolysis. *Thin Solid Films* **325**, 4–6 (1998).
53. Baroni, S., de Gironcoli, S., Dal Corso, A. & Giannozzi, P. Phonons and related crystal properties from density-functional perturbation theory. *Rev. Mod. Phys.* **73**, 515–562 (2001).
54. Giannozzi, P. *et al*. QUANTUM ESPRESSO: a modular and open-source software project for quantum simulations of materials. *J. Condens. Matter Phys.* **21**, 395502–20 (2009).
55. Hartwigsen, C., Goedecker, S. & Hutter, J. Relativistic separable dual-space Gaussian Pseudopotentials from H to Rn. *Phys. Rev. B* **58**, 3641–3662 (1998).
56. Goedecker, S., Teter, M. & Hutter, J. Separable dual-space Gaussian pseudopotentials. *Phys. Rev. B* **54**, 1703–1710 (1996).
57. Taniguchi, M., Johnson, R. L., Ghijsen, J. & Cardona, M. Core excitons and conduction-band structures in orthorhombic GeS, GeSe, SnS, and SnSe single crystals. *Phys. Rev. B* **42**, 3634–3643 (1990).
58. Hu, T. & Dong, J. Two new phases of monolayer group-IV monochalcogenides and their piezoelectric properties. *Phys Chem Chem Phys* **18**, 32514–32520 (2016).
59. Xin, C. *et al*. Few-Layer Tin Sulfide: A New Black-Phosphorus-Analogue 2D Material with a Sizeable Band Gap, Odd–Even Quantum Confinement Effect, and High Carrier Mobility. *J. Phys. Chem. C* **120**, 22663–22669 (2016).
60. Sun, J., Ruzsinszky, A. & Perdew, J. P. Strongly Constrained and Appropriately Normed Semilocal Density Functional. *Phys. Rev. Lett.* **115**, 64–6 (2015).
61. Shulenburger, L., Baczewski, A. D., Zhu, Z., Guan, J. & Tománek, D. The Nature of the Interlayer Interaction in Bulk and Few-Layer Phosphorus. *Nano Lett.* **15**, 8170–8175 (2015).
62. Chao, J. *et al*. Visible-light-driven photocatalytic and photoelectrochemical properties of porous SnSx(x = 1,2) architectures. *CrystEngComm* **14**, 3163–6 (2012).
63. Molina-Sánchez, A. & Wirtz, L. Phonons in single-layer and few-layer MoS2 and WS2. *Phys. Rev. B* **84**, 155413 (2011).
64. Chen, X., Tian, F., Persson, C., Duan, W. & Chen, N.-X. Interlayer interactions in graphites. *Sci. Rep* **3**, 693–695 (2013).
65. Björkman, T., Gulans, A., Krasheninnikov, A. V. & Nieminen, R. M. van der Waals Bonding in Layered Compounds from Advanced Density-Functional First-Principles Calculations. *Phys. Rev. Lett.* **108**, 235502–5 (2012).
66. Rydberg, H. *et al*. Van der Waals Density Functional for Layered Structures. *Phys. Rev. Lett.* **91**, 4978–4974 (2003).
67. Jung, J. H., Park, C.-H. & Ihm, J. A Rigorous Method of Calculating Exfoliation Energies from First Principles. *Nano Lett.* **18**, 2759–2765 (2018).
68. Mounet, N. *et al*. Two-dimensional materials from high-throughput computational exfoliation of experimentally known compounds. *Nat. Nanotechnol* **13**, 246 (2018).
69. Jin, K., LIU, D. & Tian, Y. Enhancing the interlayer adhesive force in twisted multilayer MoS2 by thermal annealing treatment. *Nanotechnology* **26**, 405708–405708 (2015).

Acknowledgements

This paper was supported by Konkuk University in 2019.

Author contributions

L.Y. and H.L. conceived and designed the study. M.P. performed the calculations. M.P., J.C., L.Y. and H.L. interpreted the data. All authors wrote the manuscript and approved the final version of the manuscript.

Competing interests

The authors declare no competing interests.

Additional information

Supplementary information is available for this paper at https://doi.org/10.1038/s41598-019-55577-x.

Correspondence and requests for materials should be addressed to L.Y. or H.L.

Reprints and permissions information is available at www.nature.com/reprints.

Publisher's note Springer Nature remains neutral with regard to jurisdictional claims in published maps and institutional affiliations.